NANOSYSTEMS:
PHYSICS, CHEMISTRY, MATHEMATICS

Original article

Dranik M.S., et al. *Nanosystems: Phys. Chem. Math.*, 2026, **17** (1), 97–106.
http://nanojournal.ifmo.ru
DOI 10.17586/2220-8054-2026-17-1-97-106

Self-propagating high-temperature synthesis of Zr-based ceramics from Zr–B_4C composite powder

Maria S. Dranik[1,a], Leonid D. Yagudin[1,b], Alexander I. Malkin[1,c], Svetlana V. Chizhevskaya[2,d], Alexander V. Zhukov[2,e], Galina E. Nikiforova[3,f]

[1]Frumkin Institute of Physical Chemistry and Electrochemistry of the Russian Academy of Sciences, Moscow, 119071, Russia

[2]Mendeleev University of Chemical Technology, Moscow, 125047, Russia

[3]Kurnakov Institute of General and Inorganic Chemistry of the Russian Academy of Sciences, Moscow, 119991, Russia

[a]m.dranik@yandex.ru, [b]yagudinld@icloud.com, [c]mlkn@list.ru, [d]chizhrctu@rambler.ru, [e]lexzhukov@yandex.ru, [f]gen@igic.ras.ru

Corresponding author: M. S. Dranik, m.dranik@yandex.ru

ABSTRACT The ZrB_2–ZrC ceramic powders were prepared by self-propagating high-temperature synthesis (SHS) using Zr–B_4C composite powders as a precursor. Composite powders were obtained by ball milling in hexane (3÷12 min). The structure, morphology, phase and fractional composition were investigated for both composite powders and SHS products. It was found that B_4C grains are intensively embedded in Zr, and their distribution in composite particles becomes uniform by 9 min of ball milling. The possible route of the SHS reaction is proposed.

KEYWORDS ultra-high temperature ceramics, ceramic powder, self-propagating high-temperature synthesis, ball milling, zirconium, boron carbide, zirconium diboride, zirconium carbide.

ACKNOWLEDGEMENTS The microscopic studies of the cross-sections and ceramic powders were carried out using the equipment of the JRC PMR IGIC RAS. The diffractometric studies were performed using the equipment JRC PMR IPCE RAS.
This research was funded by the Ministry of Science and Higher Education of the Russian Federation.

FOR CITATION Dranik M.S., Yagudin L.D., Malkin A.I., Chizhevskaya S.V., Zhukov A.V., Nikiforova G.E. Self-propagating high-temperature synthesis of Zr-based ceramics from Zr–B_4C composite powder. *Nanosystems: Phys. Chem. Math.*, 2026, **17** (1), 97–106.

1. Introduction

Transition metal diborides (MB_2, M = Zr, Hf, Ti) exhibit outstanding characteristics such as a high melting point (>3000 C), chemical resistance, excellent mechanical properties (E = 340∼560 GPa, H = 20∼35 GPa [1]), electrical and thermal conductivity. These materials retain their properties even at high temperatures (> 550 °C), are resistant to thermal shock and possess moderate thermal expansion [2]. As a result, they found application in ultrahigh-temperature ceramics (UHTC) [3–5]. To obviate the limitations of single-phase UHTC, they are alloyed with various additives: carbides [6, 7], nitrides [8, 9] and silicides [10, 11] of transition metals, Mo, W, Ta and Si [12, 13], as well as SiC. In particular, the development of ZrB_2–ZrC composite ceramics allows for reducing their brittleness and increasing damage resistance [14].

Self-propagating high-temperature synthesis (SHS) is a common method for ZrB_2 synthesis. This process is faster and less energy-consuming than traditional techniques [15–18]. Its products demonstrate excellent sinterability and remarkable mechanical properties. Johnson *et al*. [19] proposed to obtain ZrB_2–ZrC ceramic composite using Zr–B_4C as a reaction system. They managed to produce a non-porous material via the directed reaction of Zr with porous B_4C at 1900°C in an argon atmosphere. The product represented a composite, consisting of ZrC_x and residual metal matrix reinforced with ZrB_2 platelets. A more recent study by Hu *et al*. [20] compares the characteristics of products derived from Zr–B_4C and Al–Zr–B_4C systems using SHS in an argon atmosphere. In both cases, mixtures of ZrB_2 and ZrC were obtained. Along with Al, other metals, such as Ni [21] and Cu [22], which prevent particle agglomeration, are often considered. The possibility of producing ZrB_2–ZrC in air was discussed in Tsuchida and Yamamoto study [23], for the Zr/B/C powder mixture. After that, research in this area was not continued. All these investigations aim to reduce particle size and decrease the cost of synthesis. Preliminary ball milling of the initial powders may also help to achieve these

© Dranik M.S., Yagudin L.D., Malkin A.I., Chizhevskaya S.V., Zhukov A.V., Nikiforova G.E., 2026

goals. However, such a synthesis route, which includes preliminary mechanical treatment and subsequent SHS, is poorly studied.

In this paper, ZrB_2–ZrC ceramic powders were obtained using Zr–B_4C composite powders prepared by ball milling. For the first time, such ceramic powders were produced via SHS in air. The influence of preliminary ball milling on the composite powders and the SHS products is considered. These results may be of interest for developing means to reduce the cost of manufacturing UHTC ceramics. The promising directions of further exploration are also established.

2. Materials and Methods

2.1. Synthesis of ZrB_2–ZrC ceramic powders

The composite powders were prepared using boron carbide (grade F1200, $\omega(B_4C)$ = 95.0 wt. %, D_{av} = 4.8 mm, TS 3988-002-64050283-2013) and zirconium (grade PtZrK-1, $\omega(Zr) \geq$ 96.8 wt. %, D_{av} = 12.3 mm, TS 48-4-234-84) powders. The vacuum-dried (50 mbar, 180°C, 8 h) initial reagents were mixed in stoichiometric ratio, i.e. 83:17 by weight.

The mechanical treatment of the initial mixture was carried out in water-cooled AGO-2U planetary ball mill using hexane (95 %) medium for $\tau = 3 \div 12$ min. The mixture load consisted of 10 g and the balls load was 120 g. Solid-to-liquid ratio was 1:1.5. The balls and vials are manufactured from steel. The resulting composite powders were separated from the balls and dried in air (1 h). The samples were pressed into tablets (d = 1.0 mm, m = 1 g, P = 30 MPa) and heated using a nichrome spiral in air until they self-ignited ($\sim$300°C). The ceramic cake was ground into a homogeneous powder using an agate mortar and ethanol medium.

2.2. Phase composition, structural and morphological characteristics

The structure and morphology of composite powders dispersed on a conductive adhesive tape were examined by scanning electron microscopy using JSM-6460LA (JEOL) equipped with EDX detector.

The microstructure of composite powders, as well as the morphology of SHS products, was investigated in cross-sections with a focused ion beam scanning electron microscope TESCAN AMBER. The composite powders were mixed with a bakelite conductive resin and hot-pressed. The resulting cross-sections were sanded and cleaned of abrasive particles in an ultrasonic bath.

The phase composition of the samples was determined using an Empyrean (Malvern) X-ray diffractometer with a Ni-filtered copper anode (λ(CuKα) = 1.5418 Å) in angular ranges of 20–60° (for composite powders) and 20–80° (for ceramic powders). Crystalline phases were identified using ICDD PDF-2 database. Full-profile analysis of the X-ray patterns was performed utilizing the BGMN algorithm implemented in the Profex software package.

The fractional composition of the samples was examined with a Winner2308A laser particle analyzer (Jinan Winner Particle Instrument). Distilled water was used as the measurement medium for the composite powders, isopropyl alcohol – for the SHS products.

3. Results and Discussion

3.1. Phase composition of Zr–B_4C composite powder

The formation of composite powders involves several interrelated processes: embedding hard B_4C grains in plastic Zr particles, cold welding and crushing. According to XRD data (Fig. 1), in course of the mechanical treatment of Zr and B_4C mixture mechanosynthesis also occurs. Cubic phases containing light elements (C, H), such as Zr hydride (PDF 3-65-6972) and carbohydride (PDF 1-89-2578), are formed. The X-ray patterns also indicate the presence of α–Fe (PDF 6-0696) contamination, caused by wear of the balls and vials of planetary mill. The samples also comprise m-ZrO_2 (PDF 1-78-0047) and t–ZrO_2 (PDF 1-80-0784) present as an oxide film on the particles of initial Zr powder.

It is important to note that, due to the formation of a significant fraction of amorphous phases, full-profile analysis does not provide a satisfactory level of accuracy. Despite this fact, we can establish general patterns of mechanosynthesis and evolution in the Zr crystal structure during ball milling. The treatment duration (hereinafter – τ) increase expectedly leads to a significant rise in Zr carbohydride content from $\sim$2.43 to $\sim$57.1 wt. % (Fig. 2a). Alongside, the metallic Zr content decreases tenfold. Mechanosynthesis is obviously associated with the mechanical destruction of hydrocarbons adsorbed on fresh metal surfaces during mechanical treatment in hexane. Its mechanisms will be discussed in detail elsewhere.

Zr undergoes significant mechanical deformation during ball milling, which leads to a rapid decrease in the size of coherent scattering regions (D_{CSR}) from $\sim$154 to $\sim$56 nm ((001) axe) within 3 min of treatment (Fig. 2b). The formation of Zr-based phases and accumulation of microstrain also influence D_{CSR}. At τ = 12 min, it reaches a minimum value of $\sim$14 nm.

Slight variations in the ratio of the relative intensities of B_4C reflections may indicate its partial decomposition into graphite and a boron-enriched carbide phase. However, this assumption requires additional study.

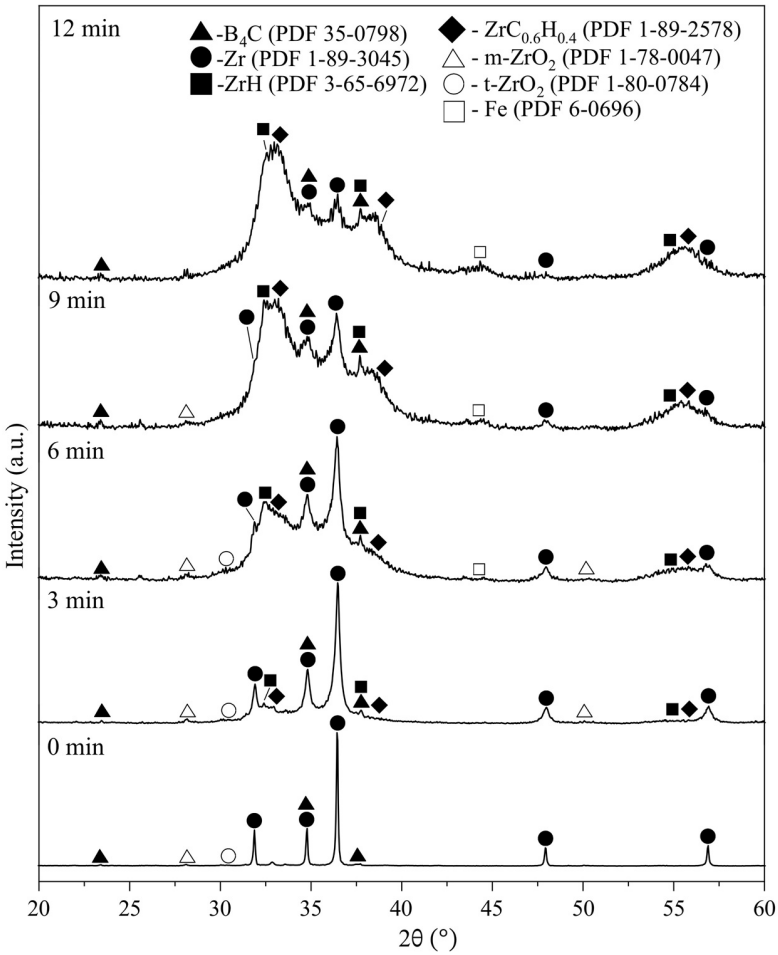

FIG. 1. X-ray diffraction patterns of Zr–B_4C composite powders obtained at τ = 0÷12 min

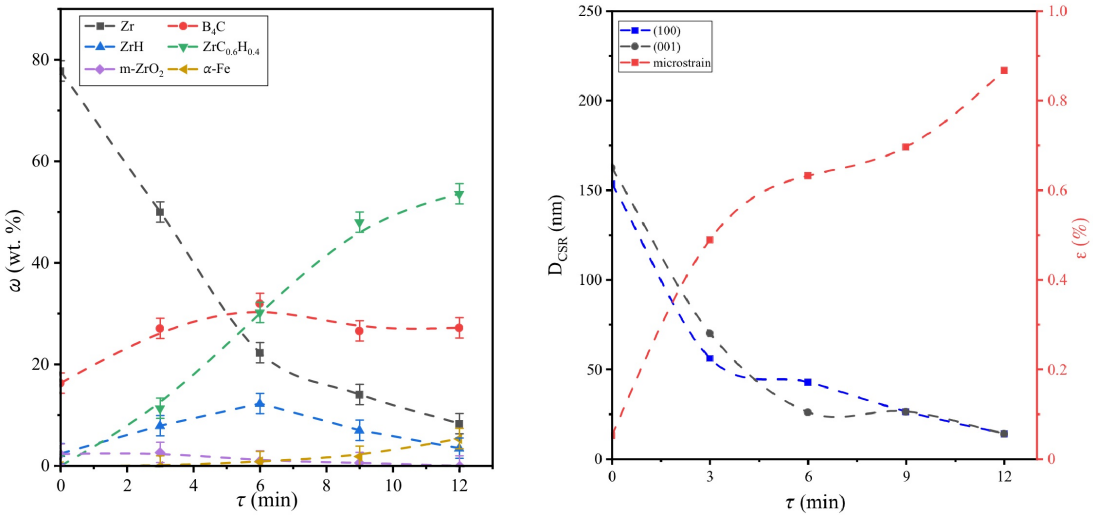

FIG. 2. Dependencies of the phase composition of Zr–B_4C composite powders (a), D_{CSR} and microstrain of Zr phase (b) on τ

3.2. Structural and morphological characteristics of Zr–B_4C composite powder

The initial stage of ball milling ($\tau \leq 6$ min) involves intense cold welding of Zr particles and active embedding of large hard B_4C grains into a relatively plastic metal. Consequently, the composite particle size (D_{50}, median size) increases from ∼5.3 to ∼6.2 μm (Fig. 3). The treatment duration increase results in the embrittlement of the material due to plastic strain accumulation and continuous embedding of B_4C. After 12 min of treatment the composite particle size decreases and reaches ∼5 μm. At the same time, as shown by electron micrographs (Fig. 4), equiaxed particles typical of quasi-brittle fracture form both at τ = 6 and 12 min.

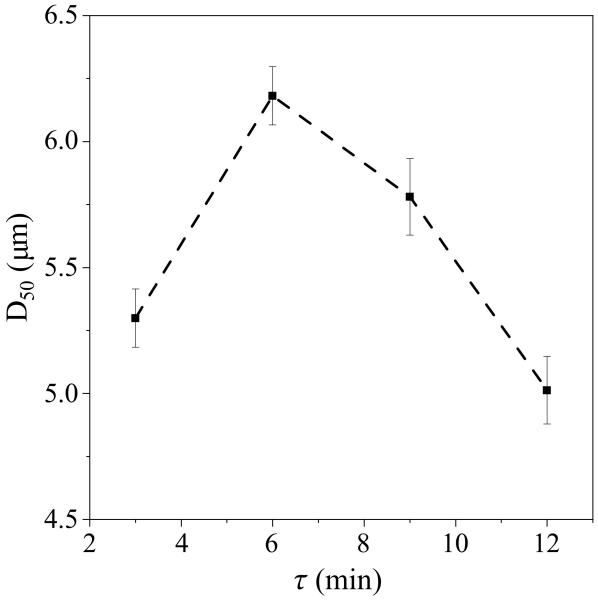

FIG. 3. Dependence of Zr–B_4C composite powder average particle size on τ

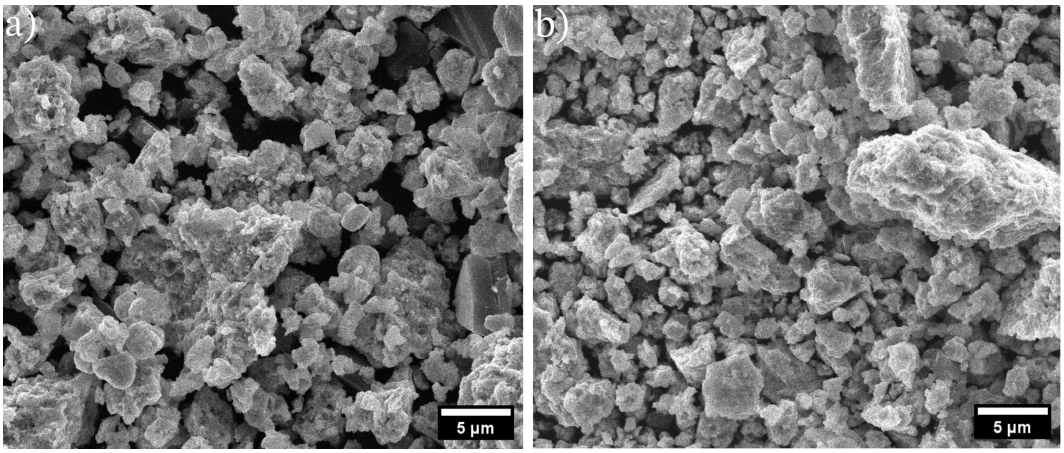

FIG. 4. SEM images of Zr–B_4C composite powder obtained at τ = 6 min (a) and τ = 12 min (b)

The investigation of composite powder cross-sections allowed us to obtain data on the distribution of B_4C inclusions within them in relation with treatment duration. As can be observed from the dependencies shown in Fig. 5, intense embedding of B_4C grains into the metal is followed by a decrease in their average size from ∼230 to ∼130 nm (Fig. 5b). Due to the aforementioned fact and as the filler (B_4C inclusions) content grows (Fig. 5a), the specific interfacial area between B_4C and Zr also increases. It is important to note that the dependence of matrix occupancy on τ shown in Fig. 5a does not consider the area of B_4C inclusions and demonstrates only their quantity in the cross-section of the composite particle. In contrast, the dependence of filler content on τ represents the ratio of B_4C inclusions area to the total particle area. Despite the tendency towards a monotonous decrease in the average size of B_4C inclusions, the dependence of their content possesses an apparent minimum at τ = 6 min. The microstructure of the samples indicates that a nearly uniform distribution of B_4C inclusions over the composite particle volume can only be achieved after 9 min of treatment (Fig. 6). The corresponding fractional composition of B_4C inclusions shown in Fig. 6c implies that almost entire mass of embedded

B_4C is concentrated in submicron-sized particles. It should be marked that the fraction of embedded micrometer-sized particles (with an initial average particle size of B_4C D_{av} = 4.8 μm) is very small.

Therefore, the embedding of large B_4C grains into the surface layers of metal is a dominant process at the initial stages of ball milling ($\tau \leq 6$ min). A further increase in treatment duration leads to the predominant crushing and migration of nanoscale B_4C grains deep into the bulk metal particle.

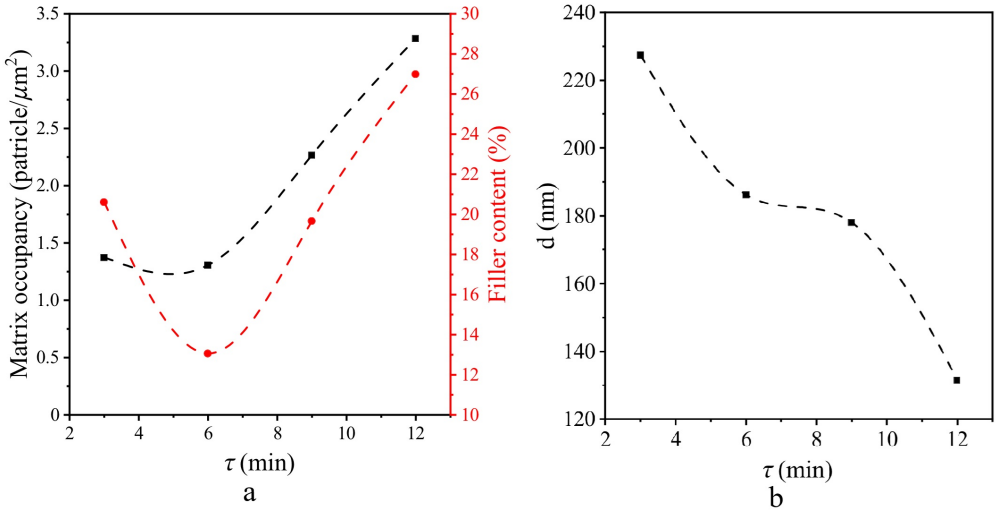

FIG. 5. Dependencies of the content of B_4C inclusions in the Zr matrix (a) and the average size of B_4C inclusions (b) on τ

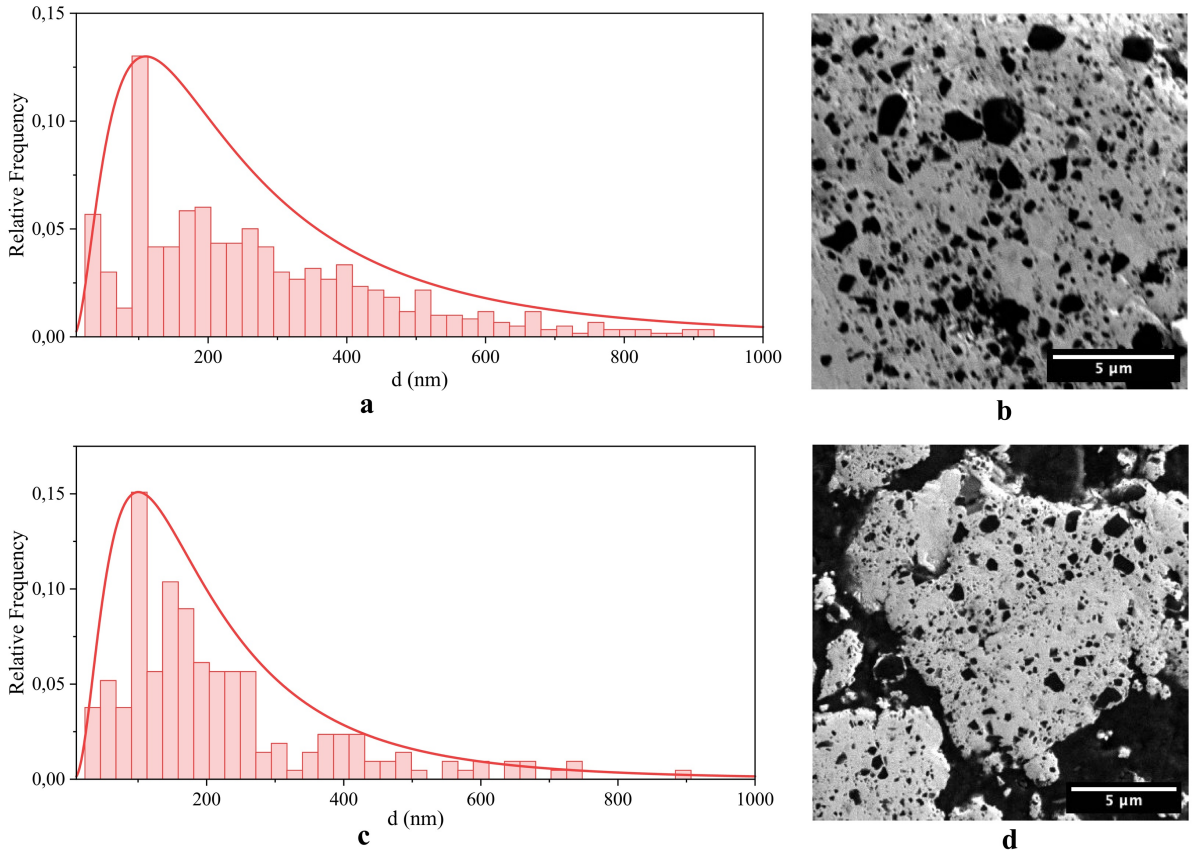

FIG. 6. Size distributions of B_4C inclusions and SEM images of Zr–B_4C composite powder cross–sections at τ = 3 min (a,b) and τ = 9 min (c,d), respectively

Obviously, B_4C inclusions are regarded as a barrier to dislocation motion. Therefore, the rise of their concentration should lead to embrittlement of Zr and, consequently, a decrease in the size of composite particles, which is confirmed

by a relevant data (Fig. 3). As follows from our studies the impact of mechanosynthesis and embedding of B_4C on the embrittling mechanism are comparable, at least for short treatment duration.

3.3. Properties of ZrB_2–ZrC ceramic powder

According to XRD data (Fig. 7), the SHS products are mainly composed of ZrB_2 (PDF 1-89-3930) and ZrC (PDF 1-89-3829) phases. Quantitative phase composition of the obtained ceramic powders is shown in Fig. 8. The samples also contain the admixtures of t-ZrO_2 (PDF 1-80-0784) and m-ZrO_2 (PDF 1-78-0047). At $\tau > 6$ min, Fe (PDF 6-0969) and FeB (PDF 1-75-1065) are also revealed. Importantly, at $\tau = 0 \div 6$ min, a small amount of unreacted Zr is present in the samples.

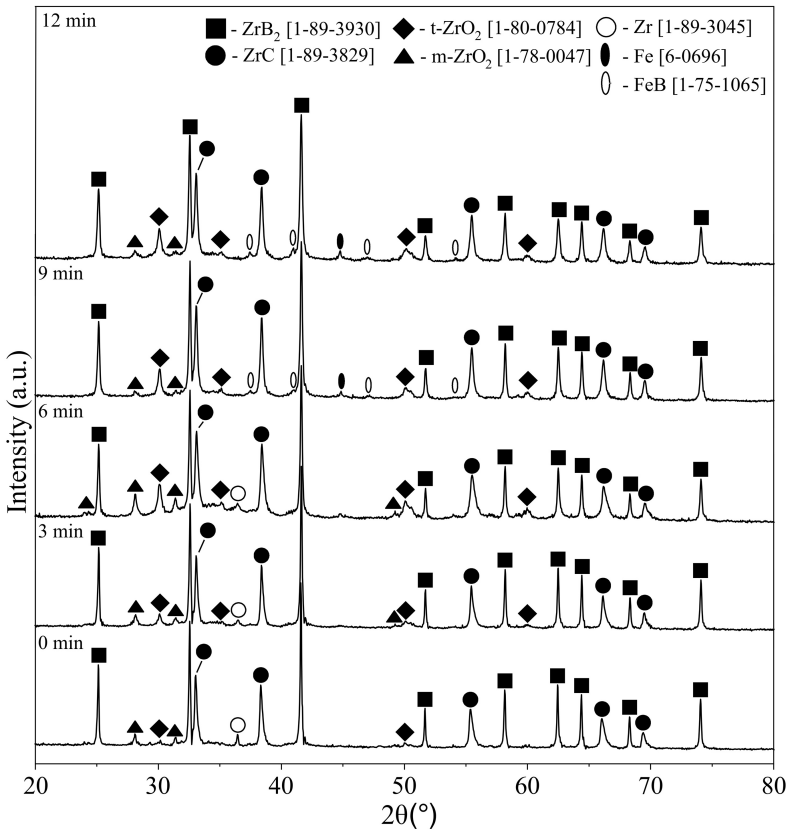

FIG. 7. X-ray diffraction patterns of SHS products obtained at $\tau = 0 \div 12$ min

The dependence of the ZrB_2 content on treatment duration exhibits a minimum corresponding to 42.3 wt. % ($\tau = 6$ min). Simultaneously, the dependence of the oxide phases total content on τ has a maximum (20.3 wt. %) at the same τ. Herewith, the ZrC content remains close to a constant value of 32.0 ± 2.5 wt. %.

Such results can be explained by the dependence of the ceramic powder composition on the characteristics of composite powders obtained at different τ. Diffraction suggests that the presence of an amorphous Zr carbohydride phase in composite powders does not significantly impact the formation of the carbide phase during SHS. A possible reason for this is the nanoscale size of the carbohydride phase and the resulting rapid oxidation. Further, at $\tau = 6$ min, composite particles are already rather coarse and contain a substantial amount of carbohydride phases, but the volume fraction of embedded B_4C is still low.

The SHS reaction is obviously a solid-state and diffusion-controlled reaction. Thus, at $\tau \leq 6$ min the diffusion of unreacted material across the product layer is hindered. In turn, this sum of factors leads to an increase in oxide impurities and a decrease in the ZrB_2 phase contents. As the distribution of B_4C inclusions in composite powders becomes uniform ($\tau \geq 9$ min), the amount of main phases increases significantly.

As expected, the accumulation of defects in the structure of composite powders leads to a decrease in D_{CSR} of the ZrB_2 phase from ∼265 nm to ∼75 nm and from ∼254 nm to ∼110 nm along (001) and (100) axes, respectively (Fig. 9a). However, the peaks of the ZrC phase exhibit anisotropic broadening at high angles. So, we cannot describe the carbide phase by considering only anisotropy of D_{CSR} and microstrain. It may be explained by the formation of non-stoichiometric carbides with different crystal lattice parameters. In the course of full-profile analysis, the carbide phase was described as a combination of carbide phases that share similar structure but possess distinct cell parameters. Fig. 9b shows the dependence of the refined carbide cell parameter on D_{CSR}.

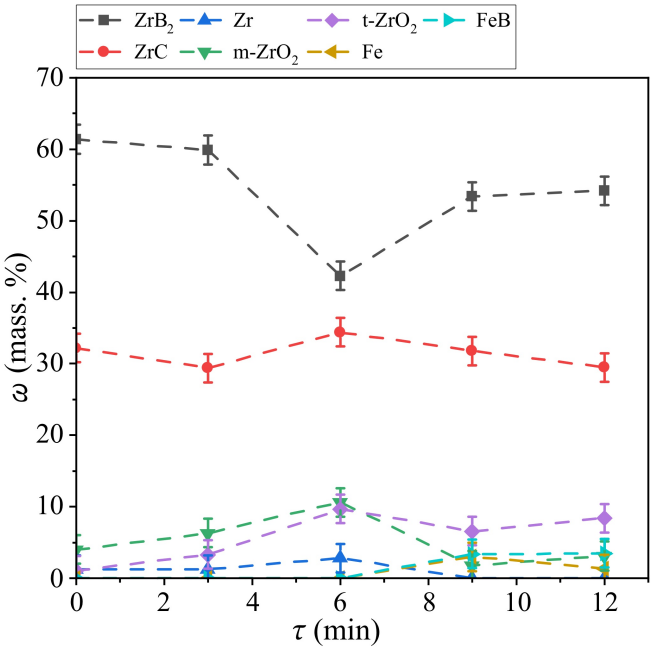

FIG. 8. Dependence of the phase mass content in SHS products on τ

The dependence of the ZrC cell parameter on its stoichiometry and the presence of impurities is well studied [24]. The change in the cell parameter due to the carbon content in pure ZrC can be described by the Mitrokhin *et al.* equation [25]. Calculation results for this equation based on experimental data are shown in the Fig. 9c. In accordance with these results, two notable observations can be made. Firstly, smaller crystallites possess a significantly smaller cell parameter, and consequently, a much lower apparent carbon content in the carbide phase. Secondly, with the C/Zr ratio values obtained (from 0.32 to 0.57), the ZrC phase with Fm-3m structure does not exist. It may indicate that the smallest crystallites represent either the ZrB phase (PDF 1-089-3932) or some non-stoichiometric Zr-based phase containing B, C, O, and N. The cell parameters of Zr-based cubic phases are very close, so their reliable identification is impossible. As the treatment duration increases the aforementioned broadening of the ZrC peaks becomes less distinct. Also the distribution of D_{CSR} and cell parameters of this phase becomes more uniform.

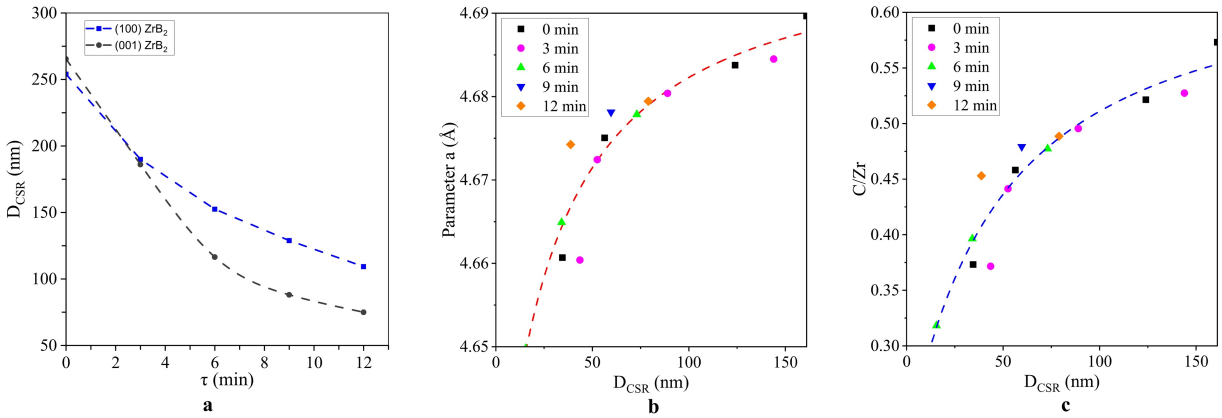

FIG. 9. Dependence of the ZrB_2 CSR size on τ (a), ZrC cell parameter a (b) and C/Zr (c)

The SHS products consist of tightly bonded aggregates of submicron spheroidal particles (Figs. 10–11), except for the sample obtained at $\tau = 0$ min. It is composed of rather dense coarse shards with an average size of ~8.4 μm (Fig. 12). The dependence of the average particle size of ceramic powders on τ is similar to that for composite powders (Fig. 13). However, ceramic particles are 1–2 μm larger.

The patterns described herein allow us to propose a mechanism for the SHS reaction in composite powders. During the solid-state SHS reaction, due to high temperatures, a solid solution of Zr, B and C is formed. Then, this homogenous phase decomposes on ZrB_2 and depleted non-stoichiometric ZrC phases. The latter forms clusters which subsequently combine, saturate with C and grow. The more uniform the distribution of B_4C in the composite powder, the finer the

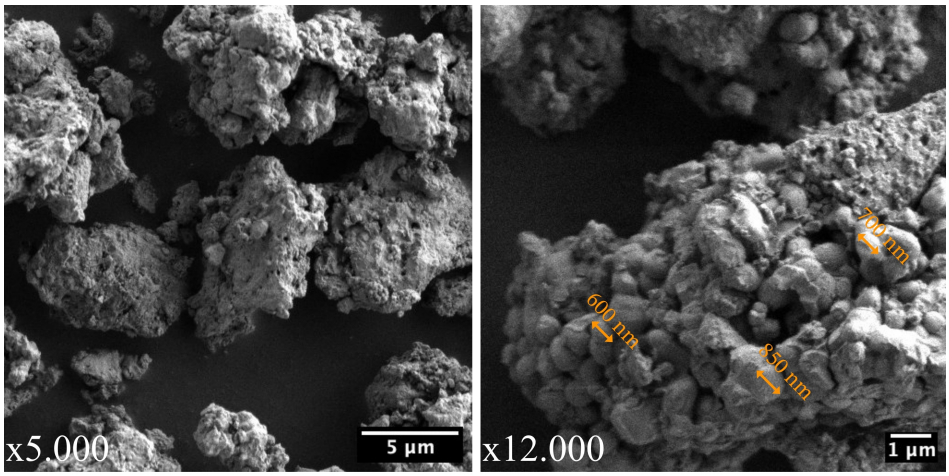

FIG. 10. SEM images of SHS product obtained at τ = 9 min at different magnification: 5.000 (a) and 12.000 (b)

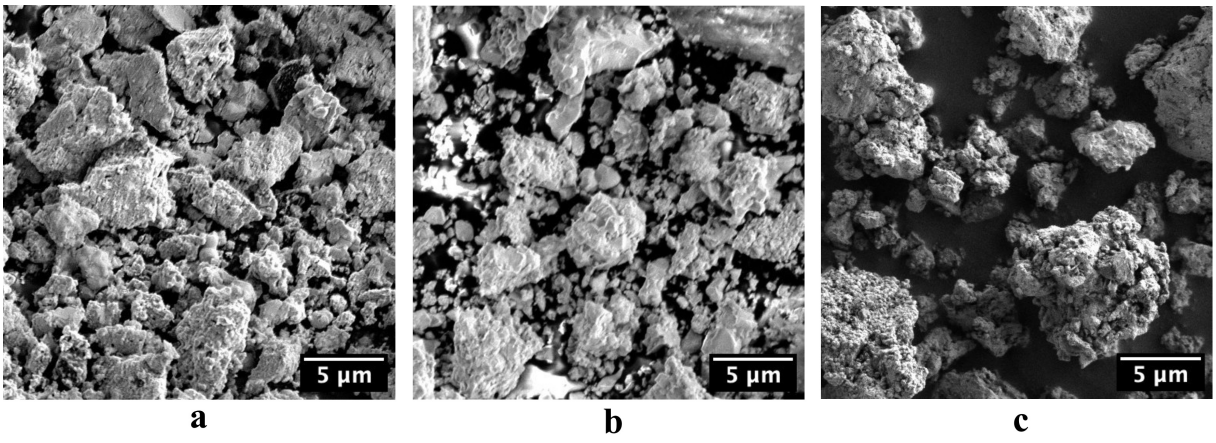

FIG. 11. SEM images of SHS product obtained at τ = 3 (a), 6 (b) and 12 (c) min

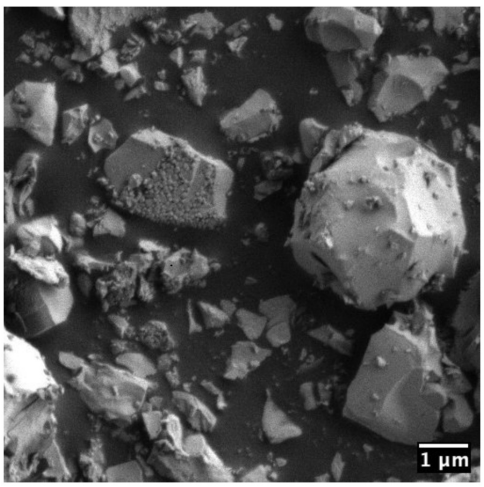

τ = 0 min, D_{50} = 8.4 μm

FIG. 12. SEM images of the SHS product obtained at τ = 0 min

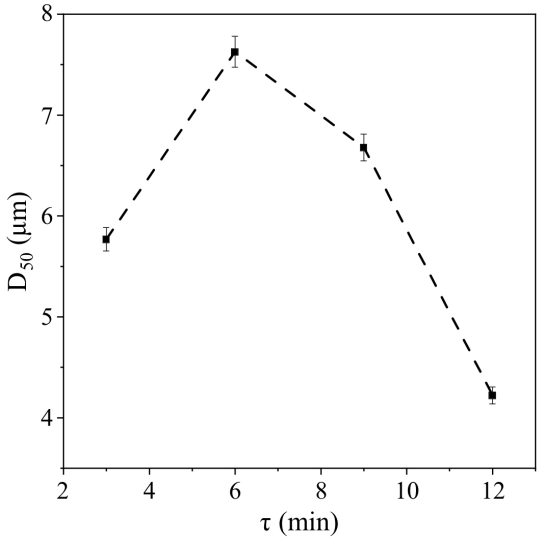

FIG. 13. The dependence of SHS product average particle size on τ

SHS products obtained. In the same way, the content of the main products should also rise. But fine product particles are easier to oxidize, so the oxide content barely decrease. Definitely, a more in-depth investigation is necessary to verify this hypothesis.

4. Conclusion

In this paper, Zr–B_4C composite powders obtained by ball milling as well as their SHS products were considered. Their structure, morphology, phase and fractional composition were investigated. Mechanochemical processes were determined to actively proceed during ball milling in hexane. As a result, Zr hydride and carbohydride phases form. The most uniform distribution of B_4C inclusions in the composite particles correspond to treatment duration of 9–12 min. During SHS in air, ZrB_2–ZrC ceramic powders with t-ZrO_2 and m-ZrO_2 admixtures are produced. They consist of tightly bonded aggregates of submicron spheroidal particles. The dependencies of the phase and fractional compositions of SHS products on the duration of treatment are obtained. The experimental results allowed us to formulate an assumption about a possible mechanism for the SHS reaction in composite powders: the formation of a solid solution and its subsequent decomposition.

References

[1] Golla B.R., et al. Review on ultra-high temperature boride ceramics. *Progress in Materials Science*, 2020, **111**, P. 100651.
[2] Pulci G., et al. High temperature mechanical behavior of UHTC coatings for thermal protection of re-entry vehicles. *Journal of thermal spray technology*, 2011, **20**, P. 139–144.
[3] Wuchina E., et al. UHTCs: ultra-high temperature ceramic materials for extreme environment applications. *The Electrochemical Society Interface*, 2007, **16** (4), P. 30–36.
[4] Pakseresht A., Mosas K.K.A. *Ceramic Coatings for High-Temperature Environments*. Engineering Materials, 2023, 491 p.
[5] Wyatt B.C., et al. Ultra-high temperature ceramics for extreme environments. *Nature Reviews Materials*, 2024, **9**(11), P. 773–789.
[6] Tiwari M., et al. The microstructural and mechanical behavior of in-situ synthesized ZrB_2–ZrC and ZrB_2–SiC–ZrC composites: A comparative study. *Vacuum*, 2023, **214**, P. 112199.
[7] Xu L., et al. In situ synthesis of ZrB_2–ZrCx ceramic tool materials toughened by elongated ZrB_2 grains. *Materials & Design*, 2013, **49**, P. 226–233.
[8] Zhao H., et al. In situ synthesis mechanism of ZrB_2–ZrN composite. *Materials Science and Engineering: A*, 2007, **452**, P. 130–134.
[9] Cheng E.J., Katsui H., Goto T. Microstructure of ZrB_2–ZrN directionally solidified eutectic composite by arc-melting. *Journal of Asian Ceramic Societies*, 2018, **6**(1), P. 102–107.
[10] Silvestroni L., Meriggi G., Sciti D. Oxidation behavior of ZrB_2 composites doped with various transition metal silicides. *Corrosion Science*, 2014, **83**, P. 281–291.
[11] Sciti D., et al. Microstructure and mechanical properties of ZrB_2–$MoSi_2$ ceramic composites produced by different sintering techniques. *Materials Science and Engineering: A*, 2006, **434**(1-2), P. 303–309.
[12] Hwang S.S., Vasiliev A.L., Padture N.P. Improved processing and oxidation-resistance of ZrB_2 ultra-high temperature ceramics containing SiC nanodispersoids. *Materials Science and Engineering: A*, 2007, **464**(1-2), P. 216–224.
[13] Zhang S.C., Hilmas G.E., Fahrenholtz W.G. Mechanical properties of sintered ZrB_2–SiC ceramics. *Journal of the European Ceramic Society*, 2011, **31**(5), P. 893–901.
[14] Rangaraj L., et al. Low-temperature processing of ZrB_2–ZrC composites by reactive hot pressing. *Metallurgical and Materials Transactions A*, 2008, **39**, P. 1496–1505.
[15] Tsuchida T., Yamamoto S. Spark plasma sintering of ZrB_2–ZrC powder mixtures synthesized by MA-SHS in air. *Journal of Materials Science*, 2007, **42**(3), P. 772–778.
[16] Qiu H.Y., et al. ZrB_2 powders prepared by boro/carbothermal reduction of ZrO_2: The effects of carbon source and reaction atmosphere. *Powder Technology*, 2012, **217**, P. 462–466.

[17] Sacks M.D., et al. Carbothermal reduction synthesis of nanocrystalline zirconium carbide and hafnium carbide powders using solution-derived precursors. *Journal of Materials Science*, 2004, **39**, P. 6057–6066.
[18] Zhang S., et al. Novel synthesis of ZrB_2 powder via molten-salt-mediated magnesiothermic reduction. *Journal of the American Ceramic Society*, 2014, **97**(6), P. 1686–1688.
[19] Johnson W.B., Nagelberg A.S., Breval E. Kinetics of formation of a platelet-reinforced ceramic composite prepared by the directed reaction of zirconium with boron carbide. *Journal of the American Ceramic Society*, 1991, **74**(9), P. 2093–2101.
[20] Hu Q., et al. Combustion and formation behavior of hybrid ZrB_2 and ZrC particles in Al–Zr-B_4C system during self-propagation high temperature synthesis. *International Journal of Refractory Metals and Hard Materials*, 2012, **31**, P. 89–95.
[21] Xu J., et al. Reaction behavior and formation mechanism of ZrB_2 and ZrC from the Ni—Zr–B_4C system during self-propagating high-temperature synthesis. *Materials*, 2022, **16**(1), P. 354.
[22] Zhang M., et al. The effect of B_4C particle size on the reaction process and product in the Cu–Zr–B_4C system, *Journal of Asian Ceramic Societies*, 2015, **3**(1), P. 38–43.
[23] Tsuchida T., Yamamoto S. Mechanical activation assisted self-propagating high-temperature synthesis of ZrC and ZrB_2 in air from Zr/B/C powder mixtures. *Journal of the European Ceramic Society*, 2004, **24**(1), P. 45–51.
[24] Gasparrini C., et al. On the stoichiometry of zirconium carbide. *Scientific Reports*, 2020, **10**(1), P. 6347.
[25] Mitrokhin V.A., Lyutikov R.A., Yurkova R.S. Change in the lattice constant of zirconium carbide in the region of homogeneity. *Inorg. Mater. (USSR) (Engl. Transl.)*, 1975, **11**(6), P. 978–980.

Submitted 26 December 2025; revised 3 February 2026; accepted 11 February 2026

Information about the authors:

Maria S. Dranik – Frumkin Institute of Physical Chemistry and Electrochemistry of the Russian Academy of Sciences, Leninskii prosp., 31.4, Moscow, 119071, Russia; ORCID 0009-0006-1953-2359; m.dranik@yandex.ru

Leonid D. Yagudin – Frumkin Institute of Physical Chemistry and Electrochemistry of the Russian Academy of Sciences, Leninskii prosp., 31.4, Moscow, 119071, Russia; ORCID 0009-0002-3000-8778; yagudinld@icloud.com

Alexander I. Malkin – Frumkin Institute of Physical Chemistry and Electrochemistry of the Russian Academy of Sciences, Leninskii prosp., 31.4, Moscow, 119071, Russia; ORCID 0000-0001-8085-7116; mlkn@list.ru

Svetlana V. Chizhevskaya – Mendeleev University of Chemical Technology, Miusskaya sq., 9, Moscow, 125047, Russia; ORCID 0000-0003-1574-7951; chizhrctu@rambler.ru

Alexander V. Zhukov – Mendeleev University of Chemical Technology, Miusskaya sq., 9, Moscow, 125047, Russia; ORCID 0000-0001-7938-0082; lexzhukov@yandex.ru

Galina E. Nikiforova – Kurnakov Institute of General and Inorganic Chemistry of the Russian Academy of Sciences, Leninskii prosp., 31, Moscow, 119991, Russia; ORCID 0000-0002-2892-6054; gen@igic.ras.ru

Conflict of interest: the authors declare no conflict of interest.